



Ga doped ZnO photonic crystals with enhanced photocatalytic activity and its reaction mechanism

Xiaofang Li, Zengzeng Hu, Jiawen Liu, Danzhen Li*, Xiaoyun Zhang, Jing Chen, Jialin Fang

State Key Laboratory of Photocatalysis on Energy and Environment, Research Institute of Photocatalysis, Fuzhou University, Fuzhou 350002, PR China



ARTICLE INFO

Article history:

Received 22 March 2016
Received in revised form 26 April 2016
Accepted 1 May 2016
Available online 4 May 2016

Keywords:

Ga doped ZnO
Photonic crystal
Slow photon
Specific surface area
Photocatalytic activity

ABSTRACT

In this study, Ga doped ZnO photonic crystals were developed for the purpose of achieving the cooperative enhancement from the photonic crystals structure and Ga doping. The Ga doped ZnO photonic crystals with highly ordered skeleton structure could be obtained via a dip-coating infiltration method. By varying the pore diameter of photonic crystals, the slow photon effect could be found over the sample with a pore diameter of 217 nm and the corresponding electronic band gap absorption was enhanced. Moreover, the introduction of Ga increased the specific surface area of Ga doped ZnO photonic crystals while the concentration of hydroxyl oxygen on the surface decreased simultaneously, which formed a competitive relationship in determining the photocatalytic performance of Ga doped ZnO photonic crystals. The photocatalytic activities for the degradation of rhodamine B showed that 3 at% Ga doped ZnO photonic crystals with a pore diameter of 217 nm exhibited higher activity compared with other samples. The higher activity could be attributed to the slow photon effect from the photonic crystal structure and increased specific surface area after Ga doping. Furthermore, based on the results of the detection of radicals, the degradation mechanism was discussed in details.

© 2016 Elsevier B.V. All rights reserved.

1. Introduction

Photocatalysis using solar energy has been considered as a promising technique in the remediation of organics contaminated environment [1–3]. As an important metal-oxide semiconductor material, ZnO was one of the promising photocatalysts that widely used in the degradation of organic pollutions. The efficiency, however, still remained at a relatively low level due to the limited absorption of solar light [4,5]. Therefore, great effort has been devoted to design ZnO photocatalysts which could exhibit higher efficiency in the utilization of solar light [6]. One was to increase the probability of photons to be absorbed by constructing multi-dimension structure in ZnO photocatalyst. Photonic crystals (PCs) were of great importance to harvest more photons under the same light intensity [7–10]. The advantage of PCs originated from their ordered structures and slow photon effects. The three-dimensional ordered structure in the PCs could not only increase the light-receiving area between photons and photocatalysts, but also facilitate the transfer of reactant molecules in the interconnected pore channels. The slow photon effect on the edge of photonic band gap slowed the propagation velocity of photons and then intensified the light absorption of photocatalysts [11]. Hence,

the design of ZnO PCs was a practical way to efficiently utilize the solar light and our previous studies have suggested that ZnO PCs could exhibit excellent photocatalytic activity [12,13].

Except for constructing PCs structure over ZnO photocatalyst, another way to improve the photocatalytic efficiency of ZnO was by doping foreign elements. Metal doping was an effective approach to modify the grain size and conductivity of ZnO, which could further influence its corresponding photocatalytic activity. The group-III atoms were considered as active foreign elements for ZnO photocatalyst because they could replace the Zn site in the ZnO matrix and another one free electron was generated [14–16]. Among group-III atoms, Ga had an ionic radius of 0.62 Å and a covalent radius of 1.26 Å, which were the closest to those of Zn (0.74 and 1.31 Å) [17]. In addition, the covalent bond length of Ga-O (1.92 Å) was similar to that of Zn-O (1.97 Å), which resulted in less lattice deformation in ZnO [18]. Therefore, Ga atom would be easier to enter the ZnO matrix and bring about changes in the properties of ZnO photocatalyst.

Herein, for the purpose of achieving the cooperatively enhanced photocatalytic efficiency that arising from both PCs structure and Ga doping, the Ga doped ZnO PCs (GZO PCs) was designed in this study. The slow photon effect resulted from the PCs structure and the role of Ga doping on the photocatalytic activity of GZO PCs for the degradation of rhodamine B were investigated in detail. Furthermore, the photocatalytic mechanism over GZO PCs was also discussed.

* Corresponding author.

E-mail address: dzli@fzu.edu.cn (D. Li).

2. Experimental

2.1. Materials

Styrene (99%) was obtained from Aldrich Co., and was further washed by 5 wt% NaOH (A.R., Sinopharm Chemical Reagent Co. (SCRC)) aqueous solution to remove the stabilizing agent (*p*-tert-butylcatechol). Potassium peroxodisulfate (A.R., SCRC) was recrystallized before use. Gallium nitrate ($\text{Ga}(\text{NO}_3)_3 \cdot x\text{H}_2\text{O}$) was purchased from Shanghai Longjin Industry & Trade Co. Zinc nitrate hexahydrate ($\text{Zn}(\text{NO}_3)_2 \cdot 6\text{H}_2\text{O}$, A.R., SCRC) and acetylacetone (A.R., SCRC) were used directly as the precursor.

2.2. Preparation of polystyrene sphere templates

The colloidal polystyrene (PS) spheres with various sphere diameters were synthesized using a typical emulsion polymerization according to the literature (Detailed experiments see in ESI) [19]. Then, the PS sphere template was deposited on the glass substrate by a solvent evaporation method. In this method, the substrate was immersed vertically into a colloidal PS suspension with a concentration of 0.05 wt% in a 50 mL beaker. Then the beaker was kept at 50 °C for about 2 days in an oven until the water was fully evaporated, leaving a PS sphere template on the substrate. Before use, the glass substrate ($1.9 \times 1.3 \text{ cm}$) was rinsed by soaking in a mixture of $\text{H}_2\text{SO}_4/\text{H}_2\text{O}_2$ solution with the volume ratio of 7:3 for 24 h, and then washed with deionized water and dried in a nitrogen stream with a flow rate of 100 mL/min. The SEM images of the as-prepared PS templates were shown in Fig. S1. The PS templates with various sphere diameters of 236, 290 and 337 nm could be obtained by using 2.4, 4.2 and 4.8 mL of styrene as the monomer, respectively. A PS template with mixed diameters was also prepared by mixing the above three spheres together and denoted as PS_{mix}.

2.3. Preparation of GZO PCs

The GZO PCs were synthesized following a dip-coating infiltration method by using the as-prepared PS templates. Firstly, the amorphous complex precursor was produced according to the literature [20]. Typically, 0.01 mol of $\text{Zn}(\text{NO}_3)_2 \cdot 6\text{H}_2\text{O}$ was dissolved in 8 mL of ethanol, and then 2 mL of acetylacetone was added. Then $\text{Ga}(\text{NO}_3)_3 \cdot x\text{H}_2\text{O}$ with different atomic ratios (1, 3, 5 and 7 at%) relative to $\text{Zn}(\text{NO}_3)_2 \cdot 6\text{H}_2\text{O}$ was added in the above solution. The resulting mixture was kept at 50 °C for 12 h until it turned into a light yellow transparent solution. After that, 10 mL of deionized water was added to the transparent solution and form the precursor. Secondly, the as-prepared PS templates were immersed vertically into the liquid precursor for 90 s to fill the void volume of the templates completely. At last, the infiltrated PS templates were dried in air at room temperature and calcined at 500 °C in air for 2 h with a heating rate of 1 °C/min to remove the PS templates and obtain the GZO PCs. For the sake of simplicity, the GZO PCs with Ga concentration of 1, 3, 5 and 7 at% were denoted as 1GZO PCs, 3GZO PCs, 5GZO PCs and 7GZO PCs, respectively. The ZnO PCs was prepared for comparison by using the same procedure but without adding the $\text{Ga}(\text{NO}_3)_3 \cdot x\text{H}_2\text{O}$ in the precursor. For comparison, a typical PS template with a diameter of 236 nm was used for the preparation of ZnO PCs and GZO PCs unless otherwise specified. An additional GZO NCs was also synthesized by employing the same method but without the PS template on the glass substrate.

2.4. Characterization

X-ray diffraction (XRD) patterns of the samples were measured by a Bruker D8 Advance X-ray diffractometer at 40 kV and

40 mA with Cu K α radiation. X-ray photoelectron spectroscopy (XPS) with monochromatized Al K α X-rays ($\text{h}\nu = 1486.6 \text{ eV}$) radiation (ThermoFisher Scientific Co. ESCALAB 250, USA) was used to investigate the surface properties. The binding energy (BE) calibration of the spectra was referred to the C1s peak located at BE = 284.6 eV for the analysis. The morphologies of the obtained samples were observed by a field-emission scanning electron microscopy (FESEM, Hitachi SU8000, operated at an accelerating voltage of 5 kV). The Brunauer–Emmett–Teller (BET) specific surface area of the samples was measured on a Micromeritics ASAP2020 analyzer by N_2 adsorption at 77 K. Diffused reflection spectra (DRS) of the samples were collected by Cary 500 UV-vis-NIR spectrophotometers with BaSO_4 as a reflectance standard. Photoelectrochemical measurement was obtained at a CHI-660D electrochemical workstation (CH Instruments, USA). The measurement was performed in a conventional three electrode cell, using Pt plate and Ag/AgCl electrode as the counter electrode and reference electrode, respectively. The working electrode was prepared on a fluorinedoped tin oxide (FTO) glass. Furthermore, 0.1 M of Na_2SO_4 solution was used as electrolyte. 5,5-Dimethyl-1-pyrroline N-oxide (DMPO) spintrapping electron spin resonance (ESR) spectra were recorded with a Bruker A300 spectrometer at room temperature. General instrument settings are as follows: microwave power, 6.35 mW; modulation amplitude, 3 G; receiver gain, 1×10^3 ; time constant, 10.24 ms; sweep time, 42 s; center field, 3507 G; sweep width, 80 G. The *N,N*-diethyl-*p*-phenylenediamine (DPD) method was employed for the detection of H_2O_2 [21]. This method was based on the horseradish peroxidase (POD)-catalyzed oxidation of DPD by H_2O_2 . The sequence of reaction led to form a pink colored •DPD⁺ radical cation. This radical cation had the absorption at 510 and 551 nm, respectively.

2.5. Test of photocatalytic activity

The photocatalytic degradation of rhodamine B (RhB) in liquid phase was carried out in a 10 mL of quartz cell. A Xe-arc lamp (500 W; Institute of Electric Light Source, Beijing, China) with various cut-off filters were used as the irradiation source. The transmitted spectra of the irradiation source were shown in Fig. S2. Typically, the GZO PCs were immersed vertically in 10 mL of the RhB aqueous solution ($5 \times 10^{-6} \text{ mol/L}$). Prior to irradiation, the solution was stirred for 20 min to reach adsorption-desorption equilibrium between the sample and RhB. As the reaction proceeded, 3 mL of RhB aqueous solution were taken at a certain time interval. The concentration of RhB was analyzed by monitoring the absorbance at $\lambda_{\text{max}} = 554 \text{ nm}$ in UV-vis spectrum with a Cary 50 UV-vis spectrophotometer (Varian Co., USA). The action spectrum was measured by bandpass filters with several representative wavelengths of $365 \pm 10 \text{ nm}$, $380 \pm 10 \text{ nm}$, $420 \pm 10 \text{ nm}$, $550 \pm 10 \text{ nm}$ and $600 \pm 10 \text{ nm}$ for evaluating the functional impact of light.

3. Results and discussion

3.1. XRD analysis

XRD patterns of the ZnO PCs and GZO PCs with different Ga concentrations were shown in Fig. 1. All diffraction peaks in the patterns could be identified as a single hexagonal phase of ZnO with zincite structure (JCPDS card no. 36-1451). The peaks at 2θ about 31.77, 34.42, 36.25, 47.54, 56.60, 62.86 and 67.96 could be indexed to the diffraction peaks of the (100), (002), (101), (102), (110), (103) and (112) crystal planes of ZnO, respectively. No characteristic diffraction peaks corresponding to Ga compound impurity could be observed either in the GZO PCs

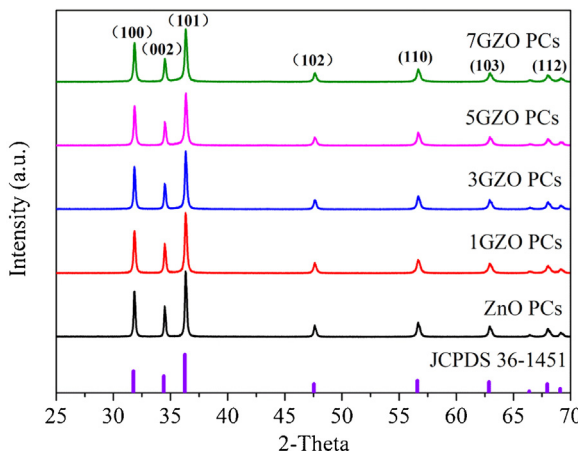


Fig. 1. XRD patterns of the ZnO PCs and GZO PCs with different Ga concentrations.

with different Ga concentrations or the GZO PCs calcinated at increasing temperature (Fig. S3). These results suggested that Ga ions have come into the crystal lattice of ZnO to substitute for Zn ions. Furthermore, it could be observed that the diffraction peak intensity of GZO PCs decreased with the increasing Ga concentration, which indicated that the increasing Ga doping concentration may lead to a decreasing grain size of GZO PCs.

3.2. XPS spectra

To obtain the chemical composition of as-prepared GZO PCs, a typical sample 3GZO PCs was further characterized by XPS measurement and the results were shown in Fig. 2a–b. All peaks in the wide-scan XPS spectrum of 3GZO PCs in Fig. 2a could be ascribed to Zn, Ga and O elements and no peaks with other elements were observed. As shown in Fig. 2b, the characteristic binding energy values of 1117.8 and 1144.7 eV for Ga 2p_{3/2} and Ga 2p_{1/2} revealed a trivalent oxidation state for gallium. The quantitative analysis of Ga concentration suggested that the actual Ga concentration in the sample 3GZO PCs was about 2.28 at%. Furthermore, it was noted that the peaks of O 1s in Fig. 2d and Zn 2p in Fig. S4 for the sample 3GZO PCs shifted slightly towards higher binding energy compared to that for the sample ZnO PCs. The shift could be attributed to the larger electronegativity of Ga³⁺ ($\chi = 1.81$) compared to Zn²⁺ ($\chi = 1.65$) [17]. These results indicated that some of the Zn²⁺ sites in the ZnO lattice have been replaced by the Ga³⁺ ions to form the Zn-O-Ga bond in the GZO PCs.

As the oxygen species were considered to be an important factor for the photocatalytic performance of ZnO, the variation in the concentration of oxygen species resulted from the doping of Ga was also discussed in this work. Fig. 2c–d and Fig. S5 showed the narrow-scan O1s XPS spectra of ZnO PCs, 3GZO PCs and 7GZO PCs, respectively. The asymmetric peaks observed in the O 1s were deconvoluted into three peaks. The peak with low binding energy (O_I) could be ascribed to the lattic oxygen in the ZnO lattice. The medium binding energy component (O_{II}) could correspond to the hydroxyl oxygen on the surface. The peak with high binding energy (O_{III}) was related with the chemically absorbed oxygen such as H₂O or O₂. Among these oxygen species, hydroxyl oxygen on the surface was a well-known source for the generation of active oxygen species responsible for the photocatalytic activity [22]. In this study, a declining intensity of O_{II} peak could be observed over GZO PCs with increasing Ga concentration, which decreased the generation of active oxygen species and was considered as an adverse factor for the photocatalytic performance of GZO PCs.

Table 1

The macropore and window pore diameters of 3GZO PCs prepared by using PS templates with different diameters.

Unit/nm	3GZO PCs/217	3GZO PCs/280	3GZO PCs/306
PS	236	290	337
Macropore	217	280	306
Window pore	75 × 59	82 × 72	85 × 66

Table 2

The macropore and window pore diameters of GZO PCs with different Ga concentration by using the same PS template with diameter of 236 nm.

Unit/nm	ZnO PCs/228	1GZO PCs/222	3GZO PCs/217	5GZO PCs/214	7GZO PCs/210
Macropore	228	222	217	214	210
Window pore	84 × 76	76 × 68	75 × 59	65 × 61	53 × 49

3.3. SEM analysis

By using the PS templates shown in Fig. S1, a typical sample 3GZO PCs with various pore diameters were prepared and the SEM images were shown in Fig. 3. It could be observed in Fig. 3a–c that 3GZO PCs well duplicated the highly ordered structure of PS template to form an ordered skeleton structure. The skeleton structure was composed of well-arranged spherical macropores and interconnected struts, which presented the hexagonal arrangement. Furthermore, the macropores were interconnected through the window pores, which were formed due to the compact structure of PS template blocking the infiltration of precursor into the contact point of PS spheres. The macropore and window pore diameters of 3GZO PCs prepared by using PS templates with different diameters were shown in Table 1. The interconnected macropores and window pores provided a possibility to form continuous channels within the PCs structure, which could improve the light harvest and facilitate the transfer of reactant molecules in the continuous channels. For the sake of simplicity, the as-prepared PCs were denoted as 3GZO PCs/217, 3GZO PCs/280, and 3GZO PCs/306, respectively. For comparison, an irregularly porous 3GZO shown in Fig. 3d was also prepared as a reference in this study.

Furthermore, to investigate the effect of Ga doping on PCs structure, ZnO PCs and GZO PCs with different Ga concentrations were also prepared by using the same PS template with diameter of 236 nm. As shown in Fig. 4a–e, all the PCs exhibited highly ordered skeleton structure except that high Ga concentration doping led to excessive aggregates surrounding the macropores and some collapse could be observed in the structure. In addition, as marked in red circles, the nanoparticles consisted of the skeleton structure became smaller with the increasing Ga concentration. Meanwhile, the smaller nanoparticles stacked thicker wall of the macropores, which resulted in the decreasing macropore diameter and window pore diameter of GZO PCs as displayed in Table 2. For the sake of simplicity, the as-prepared PCs with different Ga concentrations by using the same PS template were labeled as ZnO PCs/228, 1GZO PCs/222, 3GZO PCs/217, 5GZO PCs/214 and 7GZO PCs/210.

3.4. BET analysis

Generally speaking, the decreasing grain size often indicated the increasing specific surface area of photocatalyst, which was in favor of promoting the photocatalytic performance. To investigated the effect of Ga doping on the specific surface area of as-prepared samples, bulk GZO PCs with different Ga concentration was prepared by a vacuum filtration method according to previous study for the BET analysis [23]. The results in Table 3 showed that the BET surface area of GZO PCs increased with the increasing Ga concen-

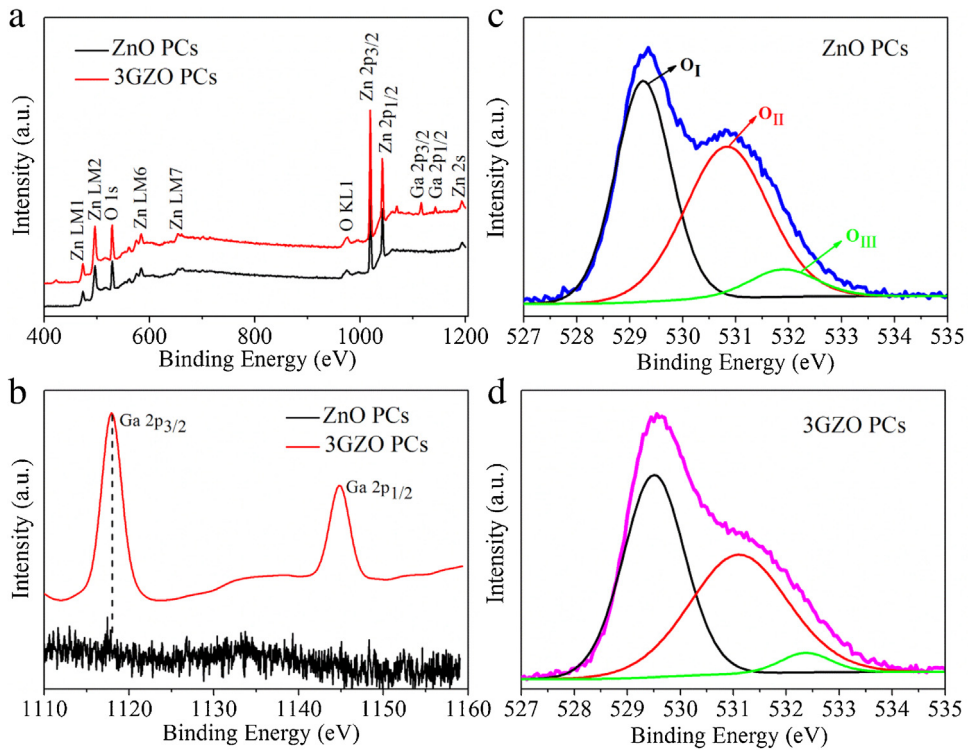


Fig. 2. (a) The wide-scan XPS spectra of 3GZO PCs and ZnO PCs. (b) The narrow-scan Ga 2p XPS spectra of 3GZO PCs and ZnO PCs. The narrow-scan XPS spectra and deconvoluted curves of the O 1s peak for the (c) ZnO PCs and (d) 3GZO PCs.

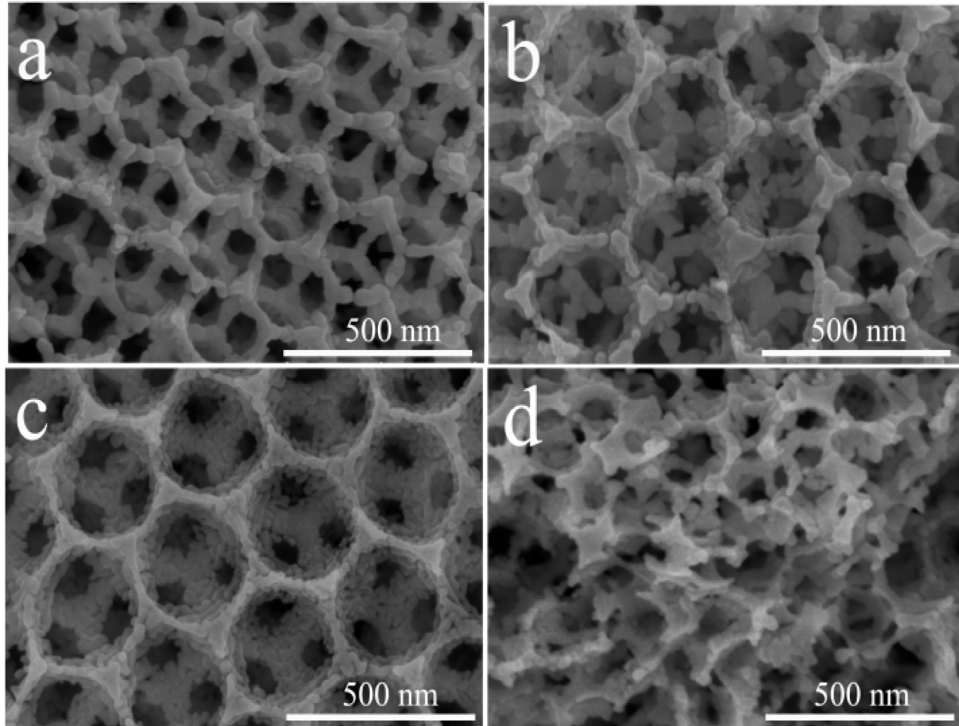


Fig. 3. SEM images of the 3GZO PCs with various pore diameters: (a) 3GZO PCs/217, (b) 3GZO PCs/280, (c) 3GZO PCs/306 and (d) porous 3GZO.

tration, which could provide more reaction sites and facilitate the photocatalytic reaction.

3.5. Spectra of reflection and absorption

The reflection spectra of a typical sample 3GZO PCs with different pore diameters were shown in Fig. 5(a). The peak at 390 nm was attributed to the electronic band gap reflection of 3GZO PCs. Furthermore, the reflection of photonic band gaps located at 485,

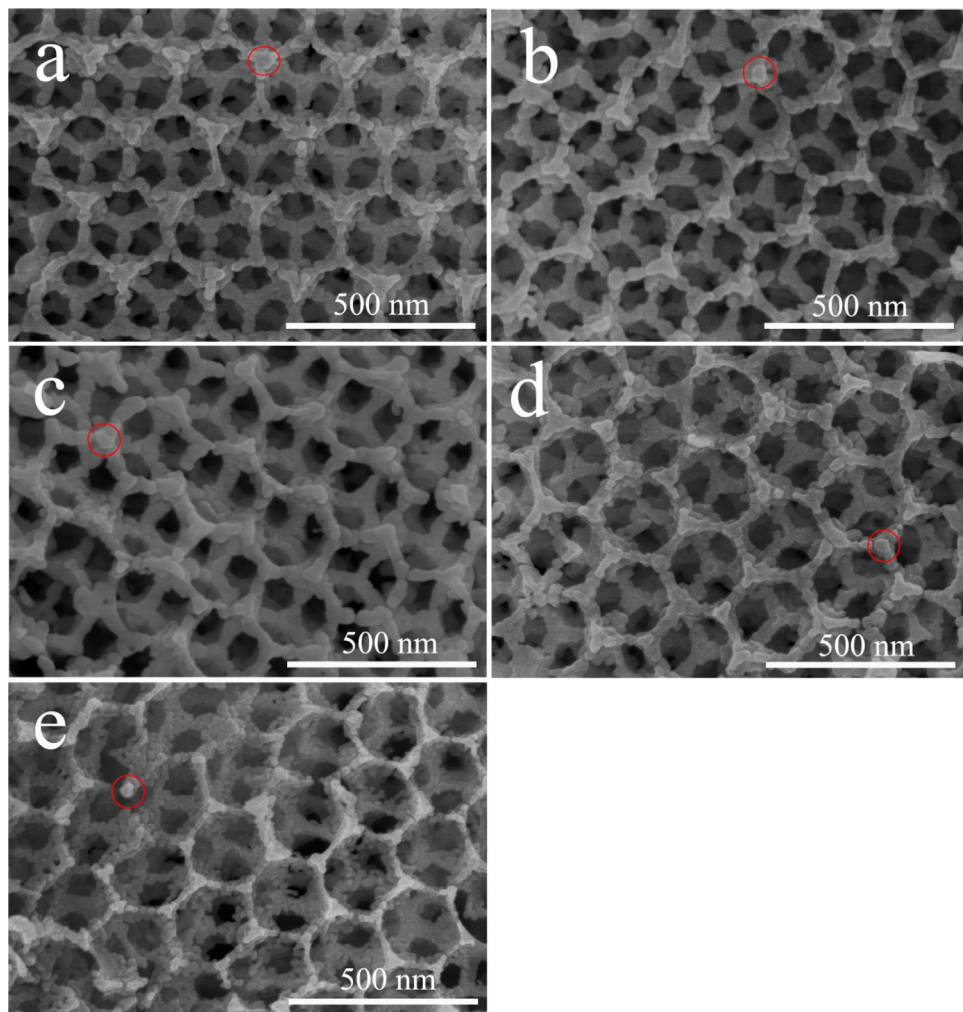


Fig. 4. SEM images of the as-prepared ZnO PCs and GZO PCs with different Ga concentrations: (a) ZnO PCs/228, (b) 1GZO PCs/222, (c) 3GZO PCs/217, (d) 5GZO PCs/214, (e) 7GZO PCs/210; (f) the changes in the pore diameters of the as-prepared samples.

Table 3
BET specific surface area of GZO PCs with different Ga concentrations.

Unit/(m ² /g)	ZnO PCs/228	1GZO PCs/222	3GZO PCs/217	5GZO PCs/214	7GZO PCs/210
BET area	15.8	18.3	19.8	21.9	24.1

Table 4
The photonic band gaps measured from the reflection spectra (PBG_{measured}) and calculated from the modified Bragg's law (PBG_{calculated}).

Unit/nm	3GZO PCs/217	3GZO PCs/280	3GZO PCs/306
PBG _{measured}	485	595	650
PBG _{calculated}	475	613	670
Deviation (%)	2.1%	3.0%	3.0%

595 and 650 nm could also be observed for 3GZO PCs/217, 3GZO PCs/280 and 3GZO PCs/306, respectively. In addition, the photonic band gap locations of 3GZO PCs could also be theoretically predicted according to the modified Bragg's law [12,24] and the detailed calculation process was shown in Fig. S6. The photonic band gaps measured from the reflection spectra and calculated from the modified Bragg's law were compared in Table 4. These results indicated that the measured photonic band gaps were approximate with the calculated values. No photonic band gap could be found due to the collapse of ordered skeleton structure for porous 3GZO. More-

over, it was noted that the electronic band gap of 3GZO overlapped the blue edge of the photonic band gap for 3GZO PCs/217. As a result, the light absorption of 3GZO PCs/217 could be enhanced due to the slow photon effect. While the photonic band gaps of the as-prepared samples 3GZO PCs/280 and 3GZO PCs/306 were far away from the electronic band gap of 3GZO, the slow photon effect would be ignored. In order to verify the slow photon effect on the electronic band gap absorption, the reflection spectra of 3GZO PCs with various pore diameters were transformed into absorption spectra by the Kubelka–Munk function and the resultant spectra was shown in Fig. 5(b). As it could be seen, light with wavelengths shorter than 390 nm could be absorbed by the as-prepared samples. Meanwhile, an absorption enhancement located at 380–390 nm in the electronic band gap absorption region was observed over 3GZO PCs/217. The enhancement could be attributed to the slow photon effect, which slowed the light propagation in the 3GZO PCs and thus reinforced the interaction between photons and the 3GZO.

As Ga doping narrowed the pore diameter of as-prepared PCs, the location of photonic band gap, which was directly related to the pore diameter of PCs, would be affected. To verify the effect of Ga doping on photonic band gap of as-prepared PCs, reflection spectra of ZnO PCs and GZO PCs with different Ga concentration were shown in Fig. 6. As it could be seen, the electronic band gap reflection of GZO PCs remained unchanged compared with ZnO PCs. Besides, when the doping concentration of Ga was below 3 at%,

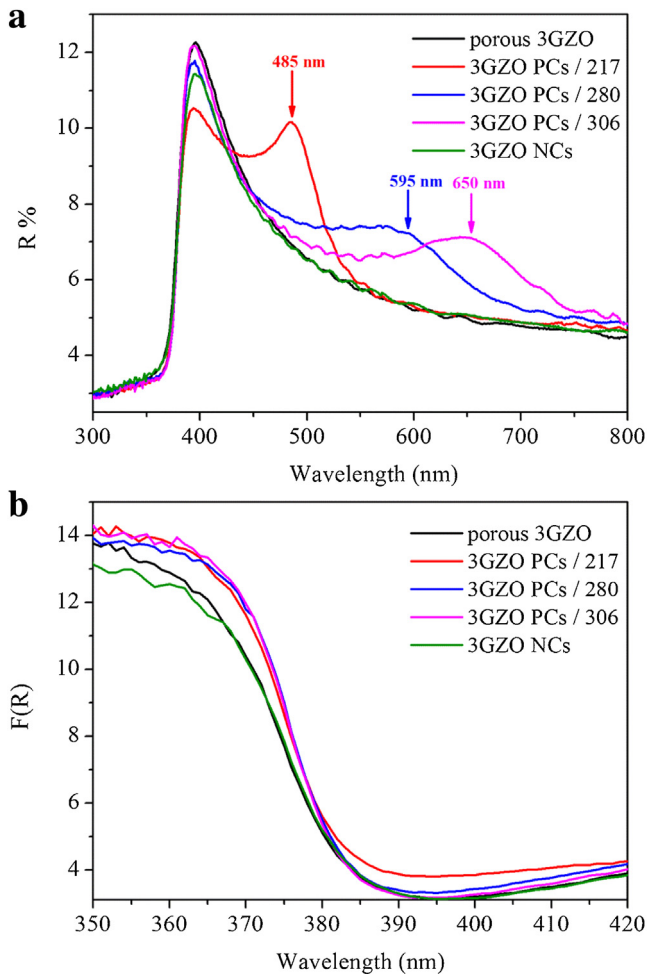


Fig. 5. (a) Reflection spectra of 3GZO PCs with various pore diameters in the present of water and (b) absorption spectra of as-prepared 3GZO PCs transformed from corresponding reflection spectra by using the Kubelka-Munk function.

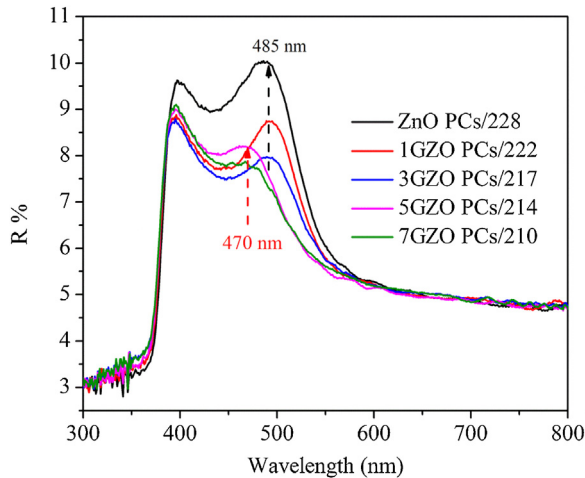


Fig. 6. Reflection spectra of the ZnO PCs and GZO PCs with different Ga concentration in the present of water.

the photonic band gaps of ZnO PCs/228, 1GZO PCs/222 and 3GZO PCs/217 was similarly at 485 nm. Further increase in Ga concentration blue shifted their corresponding photonic band gaps and the photonic band gaps of 5GZO PCs/214 and 7GZO PCs/210 was located at 470 nm, which could be ascribed to the decreasing pore

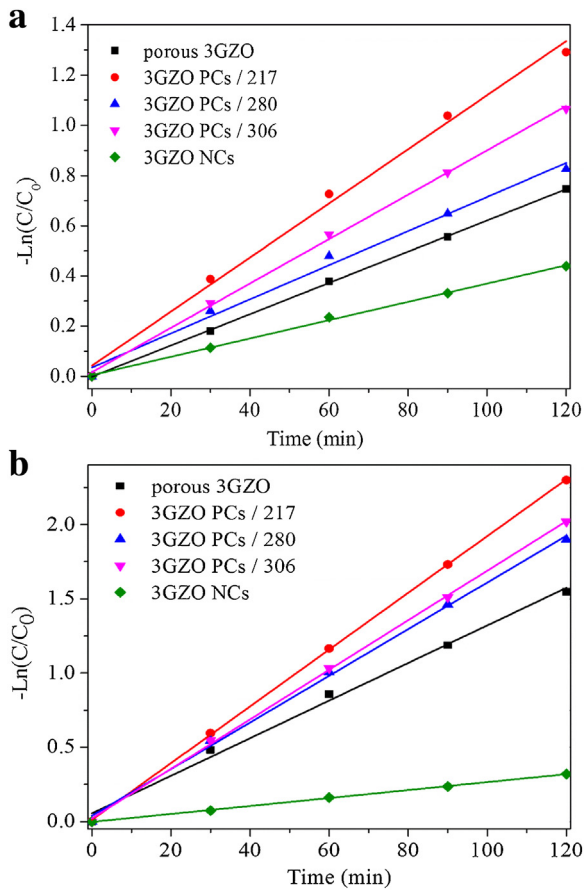


Fig. 7. Photocatalytic activities of the 3GZO PCs with various pore diameters for the degradation of RhB under light irradiation in wavelength of (a) 320–400 nm (a) and (b) 320–800 nm.

diameters of PCs. Based on the analysis in Fig. 5, the electronic band gap absorption of ZnO PCs/228, 1GZO PCs/222 and 3GZO PCs/217 could be enhanced due to the slow photon effect. As the photonic band gap of 5GZO PCs/214 and 7GZO PCs/210 got closer to their electronic band gap, the slow photon effect on enhancing the absorption would be boosted.

3.6. Slow photon effect on the photocatalytic activity of GZO PCs

To demonstrate the slow photon effect on the photocatalytic activity of GZO PCs, the activities of 3GZO PCs with various pore diameters for the degradation of RhB under UV light irradiation in wavelength of 320–400 nm were first shown in Fig. 7(a). The degradation of RhB over the porous 3GZO and 3GZO NCs were also carried out under the same conditions for comparison. As shown in Fig. 7(a), the 3GZO PCs and porous 3GZO, which were porous samples, exhibited higher catalytic activities than that of 3GZO NCs. Their higher catalytic activities could be ascribed to the enhanced light harvest in the porous structures and the facilitated mass transport in the interconnected channels. In addition, the 3GZO PCs showed better photocatalytic activities compared with the porous 3GZO, which could be attributed to the efficiently facilitated mass transport on the reaction sites resulted from the highly ordered channels with excellent connectivity. Meanwhile, it was noted that the 3GZO PCs/217 with enhanced electronic band gap absorption exhibited the highest photocatalytic activity among all the 3GZO PCs. For the samples 3GZO PCs/280 and 3GZO PCs/306, no enhancement could be observed in the electronic band gap absorption and their activi-

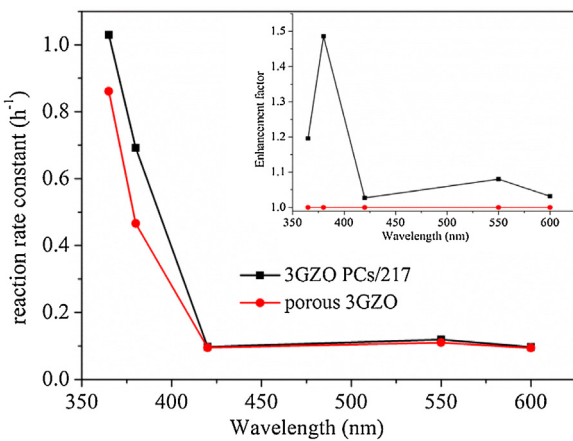


Fig. 8. The action spectra and activity enhancement spectra of 3GZO PC/217 and porous 3GZO.

ties decreased with the decreasing pore diameter, which has been proved by our previous work [20,25,26].

After demonstrating the slow photon effect under the UV light irradiation, we moved to address it under simulated solar light irradiation in wavelength of 320–800 nm. As it could be seen in Fig. S7, the overall activity under solar light irradiation could be roughly divided into two parts: the activity resulted from the electronic band gap excitation in wavelengths of 320–400 nm dominated and a small part of the activity was due to the dye sensitization in wavelengths of 400–800 nm. Therefore, as shown in Fig. 7(b), the photocatalytic activities under simulated solar light irradiation were similar with that under UV light irradiation and 3GZO PCs/217 exhibited best activity, which could be ascribed to the slow photon enhancement. Furthermore, without slow photon enhancement, the activity resulted from the dye sensitization over 3GZO PCs/217 was lower than that over other PCs in Fig. S8, which further implied that slow photon effect was responsible for the higher photocatalytic activity of 3GZO PCs/217. To further verify the origin of the activity enhancement of 3GZO PCs/217, the action spectrum of 3GZO PCs/217 and porous 3GZO was shown in Fig. 8. The activity enhancement spectrum of 3GZO PCs/217 in the inset was present by normalizing the action spectrum of 3GZO PCs/217 to that of porous 3GZO, which was used to show the activity under which wavelength of light was enhanced most in the degradation of RhB. By comparing the action spectrum and the absorption spectrum of 3GZO PCs/217, it could be concluded that the activity of 3GZO PCs/217 under light irradiation of 380 ± 10 nm was improved most and the improved activity was attributed to the enhanced electronic band gap absorption resulted from the slow photon effect. Moreover, the photodegradation stability of 3GZO PCs/217 was shown in Fig. S9. As it can be seen, 94% of the photocatalytic activity was maintained after three cycles, which indicated a relatively stable activity of 3GZO PCs/217.

3.7. Effect of Ga doping on the photocatalytic activity of GZO PCs

To evaluate the effect of Ga doping on the photocatalytic activity of as-prepared PCs, the degradation of RhB over GZO PCs with different Ga concentrations were investigated. As discussed above, three factors influencing the photocatalytic performance of GZO PCs existed after Ga doping. One was the varied location between electronic band gap and photonic band gap of GZO PCs. Furthermore, the increasing specific surface area and decreasing concentration of hydroxyl oxygen on the surface formed a competitive relationship in determining the photocatalytic performance of GZO PCs. To distinguish the three effects, porous GZO with differ-

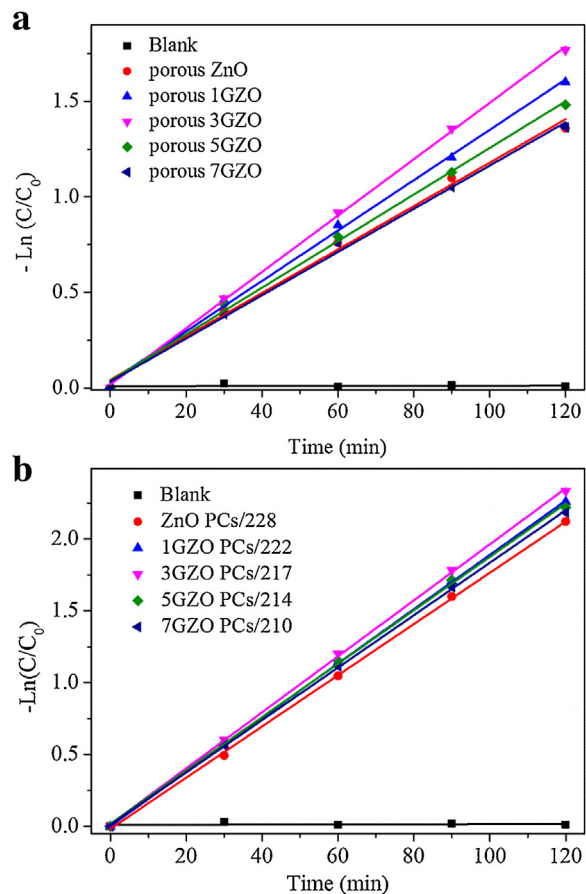


Fig. 9. Photocatalytic activities of porous GZO (a) and GZO PCs (b) with different Ga concentrations for the degradation of RhB under light irradiation in wavelength of 320 nm to 800 nm.

ent Ga concentrations as a representative of non-PCs were used for comparison. As shown in Fig. 9, when Ga concentration was below 3 at%, the photocatalytic activity of both GZO PCs and porous GZO increased with the increasing Ga concentration. Further increasing the doping concentration led to a decrease in the activities of both GZO PCs and porous GZO. However, different from porous 5GZO and 7GZO, 5GZO PCs/214 and 7GZO PCs/210 did not exhibit an obvious decrease in their photocatalytic activities with the increasing Ga concentration. For ZnO PCs/228, 1GZO PCs/222 and 3GZO PCs/217, their locations of photonic band gap were similar. Therefore, the increasing activity could be attributed to the increasing specific surface area, which could provide more reaction site and has been confirmed by previous studies [16,18]. However, the increasing surface area did not bring about sustainable growth in the photocatalytic activity of 5GZO PCs/214 and 7GZO PCs/210, which indicated that the decreasing concentration of hydroxyl oxygen on the surface became a dominating factor in the photocatalytic activity of GZO PCs with high Ga concentration. Due to the decrease in concentration of hydroxyl oxygen, less active oxygen species could be generated. Therefore, the photocatalytic activities of 5GZO PCs/214 and 7GZO PCs/210 decreased. While a blue shift could be observed in the photonic band gaps of 5GZO PCs/214 and 7GZO PCs/210, which would further enhance their electronic band gap absorption due to the boosted slow photon effect. Benefited from this compensation, the photocatalytic performance of 5GZO PCs/214 and 7GZO PCs/210 were different from that of porous 5GZO and porous 7GZO.

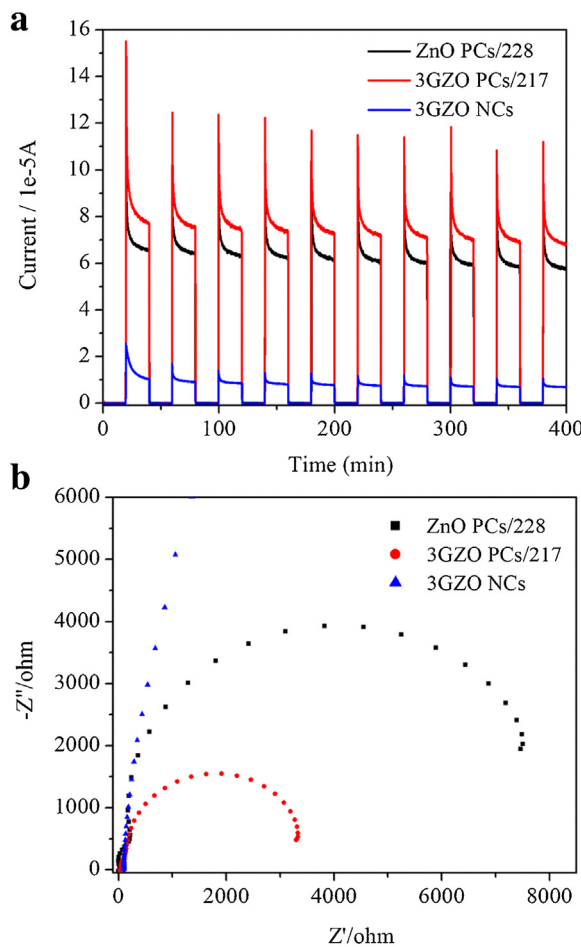


Fig. 10. (a) Transient photocurrent response and (b) EIS Nyquist plots without any bias potential of the as-prepared samples under light irradiation in wavelength of 320 nm to 800 nm.

3.8. Enhancement of interface charge separation efficiency

Photoelectrochemical measurement was performed over the 3GZO PCs/217 to further investigate the enhancement mechanism for the photocatalytic activity. The obtained photocurrent-time ($I-t$) profiles without any bias potential were shown in Fig. 10a. Compared to 3GZO NCs, sample 3GZO PCs/217 exhibited remarkably strong photocurrent intensity. The highly ordered skeleton structure and enhanced electronic band gap absorption of 3GZO PCs/217 were the main reasons for the higher photocurrent. Furthermore, the photocurrent of 3GZO PCs/217 was higher than that of ZnO PCs/228 due to the increased surface area after Ga doping. Electrochemical impedance spectroscopy (EIS) in Fig. 10b was also used to evaluate the separation efficiency of photogenerated charges on 3GZO PCs/217. The radius of the arc on the EIS Nyquist plot represented the charge transfer step occurring at the surface of the electrode. The result of EIS plot demonstrated that the separation efficiency of photogenerated electronic-hole pairs increased in the order of 3GZO NCs < ZnO PCs/228 < 3GZO PCs/217, which was in good agreement with the photocurrent measurements. These results further confirmed the good photocatalytic activity of 3GZO PCs/217 for the degradation of RhB in the study.

3.9. Possible photocatalytic mechanism

Generally, photo-induced holes, $\cdot\text{OH}$ radicals and $\cdot\text{O}_2^-$ radicals were considered to be main active species for the organic pollu-

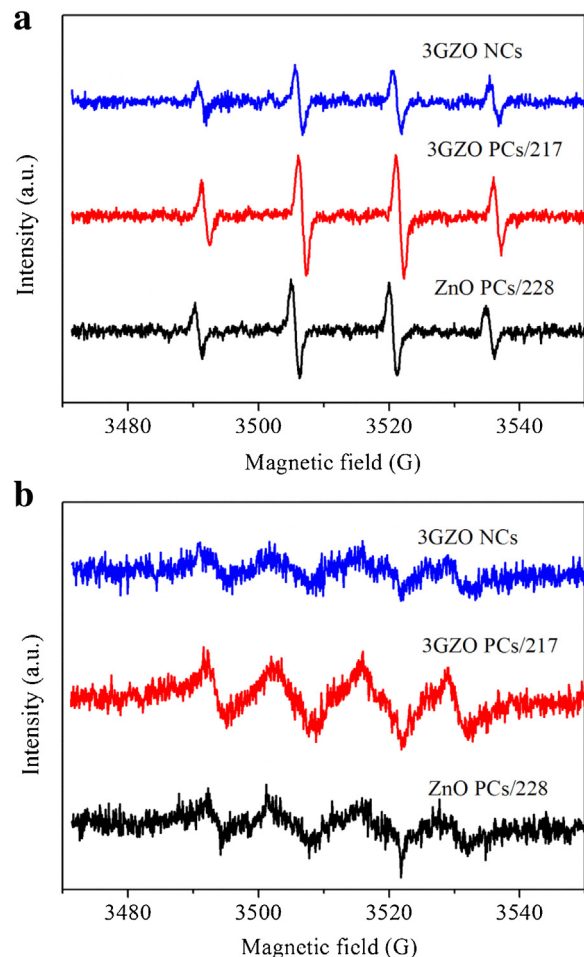


Fig. 11. DMPO spin-trapping ESR spectra of the as-prepared samples (a) in aqueous dispersion for DMPO- $\cdot\text{OH}$ and (b) in methanol dispersion for DMPO- $\cdot\text{O}_2^-$ under light irradiation in wavelength of 320–800 nm.

tants degradation. Photo-induced holes could be generated by the excitation of 3GZO PCs/217. The existence of $\cdot\text{OH}$ radicals and $\cdot\text{O}_2^-$ radicals were proved by the DMPO spin-trapping ESR technique. As shown in Fig. 11, the characteristic quartet peaks of DMPO- $\cdot\text{OH}$ adduct and the characteristic sextet peaks of DMPO- $\cdot\text{O}_2^-$ adduct were observed over 3GZO PCs/217, which verified the presence of $\cdot\text{OH}$ radicals and $\cdot\text{O}_2^-$ radicals in the catalyst system. Furthermore, it was found that the intensity of $\cdot\text{OH}$ radicals and $\cdot\text{O}_2^-$ radicals over 3GZO PCs/217 were higher than that over ZnO PCs and 3GZO NCs, respectively. This result indicated that 3 at% of Ga doping and PCs structure could promote the generation of photo-induced electron-hole pairs and active radicals in 3GZO PCs/217, which further verified the higher photocatalytic activity.

To investigate the roles of these active species in photocatalytic degradation process, different types of scavengers were added. As shown in Fig. 12, the addition of CH_3OH as a hole scavenger and terb-butyl alcohol (TBA) as a scavenger for $\cdot\text{OH}$ radicals significantly inhibited the photocatalytic activity, which indicated that photo-induced holes and $\cdot\text{OH}$ radicals played the most important role in the degradation of RhB. Furthermore, benzoquinone (BQ) as ascavenger for $\cdot\text{O}_2^-$ suppressed the photocatalytic activity to a lesser extent. It was noted that the photocatalytic activity of 3GZO PCs/217 could be improved observably when the reaction was carried out under O_2 atmosphere. The presence of O_2 as an electron scavenger could trap the photogenerated electrons. As a result, more photogenerated holes, $\cdot\text{OH}$ radicals and $\cdot\text{O}_2^-$ radicals could be produced and participated in the RhB degradation.

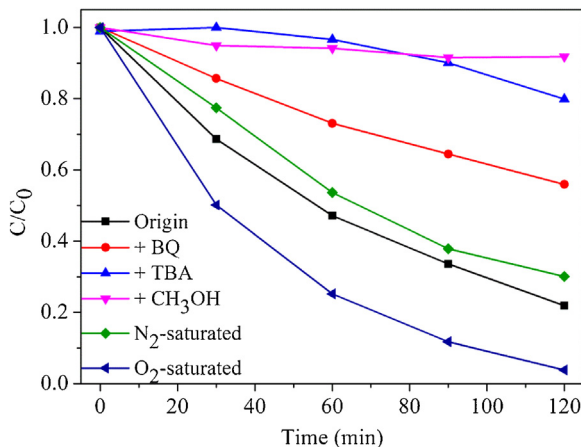


Fig. 12. Photocatalytic degradation of RhB over sample 3GZO PCs/217 with various scavengers under light irradiation in wavelength of 320 nm to 800 nm.

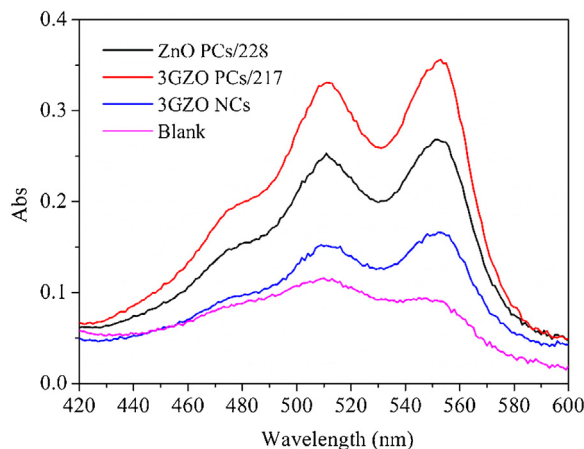
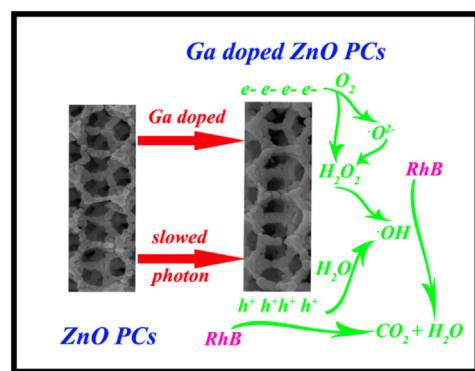


Fig. 13. UV-vis spectra of the DPD/POD reagent reacted with the produced H₂O₂ over the as-prepared samples.

By contrast, 3GZO PCs/217 exhibited relatively low activity under N₂ atmosphere. This could be attributed to the lack of dissolved O₂ under N₂ atmosphere, which aggravated the recombination of photo-induced carriers. These results further confirmed that photogenerated holes, •OH radicals and •O₂[−] radicals played important role in the degradation of RhB.

In addition, the •OH radicals could also form by the decomposition of H₂O₂. The formation of H₂O₂ could be as a consequence of the reduction reactions by the photo-induced electrons of photocatalysts ($e^- + O_2 \rightarrow O_2^-$; $2e^- + O_2 + 2H^+ \rightarrow H_2O_2$; $O_2^- + O_2^- + 2H^+ \rightarrow H_2O_2 + O_2$) [27]. H₂O₂ would further decompose into the •OH radicals ($H_2O_2 + h\nu \rightarrow 2^{\bullet}OH$). In this work, the presence of H₂O₂ was detected by the DPD method and the results were shown in Fig. 13. It was noted that the amount of H₂O₂ in the 3GZO PCs/217 system was higher than other sample systems, which indicated that more •OH radicals could also be generated. These results might further explain why 3GZO PCs/217 showed the highest photocatalytic activity for the degradation of RhB.

On the basis of above experimental results, the mechanism of RhB degradation over 3GZO PCs/217 could be illustrated in Scheme 1. By constructing PCs structure and doping with moderate concentration of Ga, the electronic band gap absorption and specific surface area of 3GZO PCs/217 was enhanced, which could facilitate the generation of photo-induced carriers and provide more active sites for the redox reactions. The photo-induced electrons on the conduction band were trapped by adsorbed molecular oxy-



Scheme 1. The proposed mechanism for the photocatalytic degradation of RhB over GZO PCs.

gen on the photocatalyst surface to produce •O₂[−] radicals and H₂O₂ molecules. The •O₂[−] radicals and H₂O₂ molecules would converted into •OH radicals by chain reactions. Further, a part of photo-induced holes could also oxidize H₂O molecules to produce •OH radicals. Both photo-induced holes, •OH radicals and •O₂[−] radicals had strong oxidative abilities, and therefore they could degrade RhB into CO₂ and H₂O.

4. Conclusion

In summary, a GZO PCs with enhanced electronic band gap absorption and specific surface area was designed for higher photocatalytic efficiency by constructing PCs structure and doping with moderated concentration of Ga. The GZO PCs was prepared by substituting Ga³⁺ ions for some of the Zn²⁺ sites in the ZnO PCs under the calcination of 500 °C. By varying the pore diameter in the PCs structure, the slow photon effect could be found over the sample with a pore diameter of 217 nm and the corresponding electronic band gap absorption was enhanced. Moreover, the introduction of Ga increased the specific surface area of GZO PCs while the concentration of hydroxyl oxygen on the surface decreased simultaneously, which formed a competitive relationship in determining the photocatalytic performance of GZO PCs. The photocatalytic activity towards RhB degradation over the as-prepared GZO PCs indicated 3GZO PCs/217 exhibited higher activity compared to other samples. The higher activity could be attributed to the slow photon effect from the PCs structure and increased surface area after Ga doping. Moreover, the enhanced interface charge separation efficiency could also be observed over 3GZO PCs/217. Based on the results of the detection of radicals, the photo-induced holes, •OH radicals and •O₂[−] radicals were considered to be the main active species responsible for the degradation of RhB over 3GZO PCs/217.

Acknowledgement

This work was financially supported by the National Natural Science Foundation of China (21173047 and 21373049).

Appendix A. Supplementary data

Supplementary data associated with this article can be found, in the online version, at <http://dx.doi.org/10.1016/j.apcatb.2016.05.002>.

References

- [1] D. Chatterjee, S. Dasgupta, J. Photochem. Photobiol. C 6 (2005) 186–205.
- [2] J.M. Herrmann, Catal. Today 53 (1999) 115–129.

[3] D. Ravelli, D. Dondi, M. Fagnoni, A. Albini, *Chem. Soc. Rev.* 38 (2009) 1999–2011.

[4] S.G. Kumar, K.S.R.K. Rao, *RSC Adv.* 5 (2015) 3306–3351.

[5] T.J. Liu, Q. Wang, P. Jiang, *RSC Adv.* 3 (2013) 12662–12670.

[6] A.B. Djurišić, Y.H. Leung, A.M.C. Ng, *Mater. Horiz.* 1 (2014) 400–410.

[7] J.I.L. Chen, G.V. Freymann, V. Kitaev, G.A. Ozin, *J. Am. Chem. Soc.* 129 (2007) 1196–1202.

[8] J.I.L. Chen, G.A. Ozin, *J. Mater. Chem.* 19 (2009) 2675–2678.

[9] J.I.L. Chen, G.V. Freymann, S.Y. Choi, V. Kitaev, G.A. Ozin, *J. Mater. Chem.* 18 (2008) 369–373.

[10] J.I.L. Chen, G.V. Freymann, S.Y. Choi, V. Kitaev, G.A. Ozin, *Adv. Mater.* 18 (2006) 1915–1919.

[11] S. Nishimura, N. Abrams, B.A. Lewis, L.I. Halaoui, T.E. Mallouk, K.D. Benkstein, J.V.D. Lagemaat, A.J. Frank, *J. Am. Chem. Soc.* 125 (2003) 6306–6310.

[12] J. Liu, J. Jin, Y. Li, H.W. Huang, C. Wang, M. Wu, L.H. Chen, B.L. Su, *J. Mater. Chem. A* 2 (2014) 5051–5060.

[13] S. Meng, D. Li, X. Zheng, J. Wang, J. Chen, J. Fang, Y. Shao, X. Fu, *J. Mater. Chem. A* 1 (2013) 2744–2746.

[14] H.M. Chiu, J.M. Wu, *J. Mater. Chem. A* 1 (2013) 5524–5534.

[15] S. Yang, C. Ge, Z. Liu, Y. Fang, Z. Li, D. Kuang, C. Su, *RSC Adv.* 1 (2011) 1691–1694.

[16] J.B. Zhong, J.Z. Li, J. Zeng, X.Y. He, W. Hu, Y.C. Shen, *Mater. Res. Bull.* 47 (2012) 3893–3896.

[17] G.C. Park, S.M. Hwang, J.H. Lim, J. Joo, *Nanoscale* 6 (2014) 1840–1847.

[18] M. Thambidurai, J.Y. Kim, J. Song, Y. Ko, H.J. Song, C.M. Kang, N. Muthukumarasamy, D. Velauthapillai, C. Lee, *J. Mater. Chem. C* 1 (2013) 8161–8166.

[19] B.T. Holland, C.F. Blanford, T. Do, A. Stein, *Chem. Mater.* 11 (1999) 795–805.

[20] X. Li, X. Zhang, X. Zheng, Y. Shao, M. He, P. Wang, X. Fu, D. Li, *J. Mater. Chem. A* 2 (2014) 15769–15802.

[21] K. Kosaka, H. Yamada, S. Matsui, S. Echigo, K. Shishida, *Environ. Sci. Technol.* 32 (1998) 3821–3824.

[22] W. Li, D. Li, Y. Lin, P. Wang, W. Chen, X. Fu, Y. Shao, *J. Phys. Chem. C* 116 (2012) 3552–3560.

[23] A. Stein, R.C. Schrodén, *Curr. Opin. Solid State Mater. Sci.* 5 (2001) 553–564.

[24] R.C. Schrodén, M. Al-Daous, A. Stein, *Chem. Mater.* 13 (2001) 2945–2950.

[25] X. Li, S. Meng, J. Xian, Y. Shao, X. Fu, D. Li, *Environ. Sci. Technol.* 47 (2013) 9911–9917.

[26] X. Zheng, S. Meng, J. Chen, J. Wang, J. Xian, Y. Shao, X. Fu, D. Li, *J. Phys. Chem. C* 117 (2013) 21263–21273.

[27] A. Fujishima, X. Zhang, D. Tryk, *Surf. Sci. Rep.* 63 (2008) 515–582.